Rapid printing of nanoporous 3D structures by overcoming the proximity effects in projection two-photon lithography

Harnjoo Kim^a, Rushil Pingali^a and Sourabh K. Saha^a*

^aG.W. Woodruff School of Mechanical Engineering, Georgia Institute of Technology, Atlanta, USA

*801 Ferst Dr, Atlanta, GA 30332, USA. Email: ssaha8@gatech.edu

Rapid printing of nanoporous 3D structures by overcoming the proximity effects in projection two-photon lithography

Large and deterministic 3D structures with nanoscale features and porosities are valuable for various applications but are challenging to print due to the proximity effects that lead to the merging of adjacently printed features. Here, this challenge has been overcome by minimizing the proximity effects in projection two-photon lithography (P-TPL), which is a high-throughput photopolymerization-based 3D printing technique. Through empirical studies and physics-based computational models, it is demonstrated that the proximity effects arise from distinct optical and chemical sources. Processing conditions that individually minimize these sources have been identified. These insights have been leveraged to generate an interspersing P-TPL technique capable of rapidly printing 3D structures with features smaller than 300 nm, pores finer than 700 nm, and at rates greater than 0.5 mm²/s per layer. As interspersing P-TPL is up to 50 times faster than conventional point-scanning TPL, it can enable the scalable printing of nanoporous 3D structures.

Keywords: direct laser writing; photopolymerization; multi-photon polymerization; femtosecond projection; nanoscale 3D printing

Subject classification codes: 3-Dimensional printing; Photopolymerization; Microfabrication

1. Introduction

Three-dimensional (3D) printing of mm to cm scale polymeric structures with nanoscale features and porosities is highly desirable for creating a variety of functional materials that can help solve societal challenges in clean energy, computing, transportation, and human health. For example, it has been demonstrated that such 3D structures can be applied to build mechanical metamaterials for extreme mechanical properties (1-4), scaffolds for biomedical applications (5, 6), photonics for information processing (7-9), and structured electrodes for energy storage (10). In general, there exists a trade-off between the rate of 3D printing and the resolution of printing because of which it is

challenging to fabricate high volumes of nanoporous 3D structures. Thus, only limited success has been achieved in transitioning these functional materials from research laboratories to real-world use. Recent works in the field of two-photon lithography (TPL)-based nanoscale 3D printing have demonstrated how one may break this trade-off by drastically increasing the throughput via parallelization of processing or rapid sequential processing, or a combination of these two approaches (11-13). Although these approaches have demonstrated the rapid printing of nanoscale features, achieving nanoscale porosities is still challenging due to the inherent proximity effects which lead to the broadening and merging of closely spaced features. Here, we focus on studying the proximity effects during projection TPL (P-TPL), which was previously developed by our team as a high-throughput parallel processing technique (11). We demonstrate how proximity effects can be overcome to rapidly print densely packed 3D structures with both nanoscale features and porosities.

TPL relies on nonlinear two-photon light absorption, which is achieved at high light intensities on the order of ~1 TW/cm², to locally polymerize features that are smaller than the size of the focused light spot (14-19). Proximity effects in TPL refer to the broadening of features that are printed in the physical proximity of other features that were either processed previously or are being processed simultaneously (20-23). Proximity effects were rarely discussed in early empirical studies of TPL that were based on the sequential point-by-point writing mechanism at low laser scanning speeds of ~1–100 μm/s (17, 18). Contemporary work has demonstrated that proximity effects are negligible at such low speeds but become significant at high scanning speeds of ~10 mm/s and higher (21). At these high speeds, densely packed features are larger than their sparser counterparts even when printed under the same processing conditions. This behaviour has been leveraged to rapidly print solid geometries for microscale optics by

merging together the closely spaced features (24). Nevertheless, printing of closely spaced fine features with nanoscale porosities is challenging at high scanning speeds (21). Proximity effects have also been observed in parallelized TPL wherein multiple points are processed at once (20, 25). In these studies, more polymerization, up to the point of uncontrolled excessive printing, has been observed in densely packed structures. Collectively, these studies highlight that achieving the printing of 3D structures with fine features and fine porosities is challenging under high throughput conditions. Thus, there is a need to investigate and overcome the proximity effects to solve this challenge.

Although proximity effects have been widely observed in TPL, these effects have not been extensively studied and their physical origins are not well understood. Consequently, it is challenging to overcome the proximity effects during printing of densely packed 3D structures with porosities finer than 1 μm. For example, it has been hypothesized that proximity effects during sequential TPL arise from the reactiondiffusion kinetics of photopolymerization (21, 22, 26, 27). Specifically, the regions in the proximity of previously processed regions of the photoresist have a lower concentration of the chemical species (such as oxygen) that terminate polymerization due to their consumption (26, 28). At low scanning speeds, diffusion of the species from other regions can replenish the lost amount; but at high scanning speeds, diffusion is too slow to replenish it. Thus, subsequent polymerization is poorly terminated which then leads to broadening of the features. Additionally, it has been hypothesized that during parallel printing, the optical properties of the beam depend on the structure being printed because of which more polymerization occurs for denser structures (20, 25). These qualitative explanations help identify those geometries that exhibit significant proximity effects and thereby avoid printing them (20, 21). However, due to the lack of

physics-based quantitative models of the underlying mechanisms, it is challenging to identify how one may modify the processing conditions to overcome the proximity effects and print the desired densely packed 3D structures.

Here, we present physics-based computational models of the optical and chemical sources of the proximity effects in P-TPL and demonstrate how the model predictions were applied to enable the printing of densely packed nanoporous 3D structures. When compared with conventional point-scanning TPL, P-TPL significantly increases the rate of printing by processing an entire 2D layer at once. This is achieved by projecting a patterned 2D light sheet comprising more than a million focused spots. A key feature of P-TPL is that the projected light sheet polymerizes only a thin layer of the photopolymer without polymerizing excess material above or below the focal plane (11). It relies on spatial and temporal focusing of femtosecond light to generate nonlinear intensity gradients along the depth direction. This focusing technique has been borrowed from the field of parallel two-photon microscopy where it has been widely used to image thin axial sections in biomaterials (29). Past demonstrations of P-TPL have been limited to printing of widely spaced features (11, 30), and the printing of nanoporous 3D structures has not yet been demonstrated. Interestingly, it has been suggested that it may be impossible to print such densely packed structures with P-TPL due to the proximity effects (12, 31, 32). Here, we quantify the proximity effects in P-TPL and demonstrate that printing of such dense structures is indeed possible via modifications to the sequence of the projected images and the processing conditions.

Specifically, we demonstrate that the optical proximity effects can be minimized by projecting sparse images whereas the chemical effects can be minimized by operating under conditions that weakly consume the dissolved oxygen in the photoresist. We have applied these results to develop an interspersing projection

technique that overcomes the proximity effects and enables printing of densely packed 3D structures, as illustrated in Figure 1. We present the optical model in Section 3.1 and the model of the photopolymerization kinetics in Section 3.2. We demonstrate, both computationally and empirically, that interspersing the features by projecting a sequence of sparse images on the same plane leads to the generation of closely spaced fine features. We demonstrate printing of 3D structures with distinct features thinner than 300 nm in width and with pores smaller than 700 nm. Therefore, our work overcomes the proximity effects and enables the printing of such dense 3D structures that were challenging to rapidly print in the past.

2. Materials and Methods

2.1. Materials

Custom photopolymer resists were synthesized by mixing polyfunctional acrylate monomers, a custom photoinitiator, and a radical inhibitor. The resist comprised a mixture of: (i) a mixture of pentaerythritol tetraacrylate, pentaerythritol triacrylate (PETA), and trimethylolpropane triacrylate that was sourced from Sigma Aldrich and had a refractive index of 1.483, (ii) bisphenol A ethoxylate diacrylate with average Mn ~468 - EO/phenol 1.5 (BPADA) that was sourced from Sigma Aldrich and had a refractive index of 1.545, (iii) 4,4'-((1E,1'E)-(2-((2-Ethylhexyl)oxy)-5-methoxy-1,4-phenylene)bis(ethene-2,1-diyl))bis(N,N-dibutylaniline) that was procured from a commercial custom chemical synthesis service provider and which was synthesized from precursors as a photoinitiator following known literature procedures (33), and (iv) additional 4-methoxyphenol (MEHQ) as a radical inhibitor. The monomer mixtures (i) and (ii) were mixed in a 35:65 ratio by weight to generate a monomer blend with a refractive index of 1.52 that closely matches the refractive index of the immersion

medium of the objective lenses. This index-matched blend was used here to achieve sharp focusing through minimization of spherical aberrations in the dip-in printing mode wherein the lens is directly dipped into the photoresist during printing (34, 35). The resists contained 0.1% by weight of the photoinitiator and 500 ppm of additional MEHQ.

2.2. P-TPL 3D Printer

3D printing was performed on a custom-built P-TPL system that is similar in design to the printer used in our past study (11). The printer was driven by a Spectra-Physics Solstice Ace ultrafast laser amplifier that generates a linearly polarized beam with a center wavelength of 804 nm, FWHM spectral bandwidth of 41 nm, a pulse width of ~35 fs, and at a repetition rate of 5 kHz. The average power of the processing beam was controlled using a series of beam splitters and neutral density filters. The commercially available Lightcrafter 6500 DMD system was used as the digital mask. It has an array of 1920×1080 pixels at a pixel-to-pixel spacing of 7.56 μm. A commercially available tube lens of focal length 200 mm was used as the collimating lens. The beam was focused using a 60×1.25 NA oil immersion objective lens (Olympus RMS60X-PFOD) that had an optical transmission efficiency of 0.73. The Gaussian beam from the laser was transformed to an approximate flattop beam using a commercially available refractive beam shaper (AdlOptica GmbH, piShaper).

2.3. 3D Printing and Development

3D printing was performed by projecting a series of 2D images into the photoresist through an oil-immersion objective lens that was dipped directly into the resist. Printing was performed with a beam that had a time-averaged power of 139 nW/pixel as measured immediately before the input aperture of the objective lens. Layered 3D

printing was performed by moving the substrate away from the lens after printing of each layer. Printing was performed on top of bare glass slides coated with a thin layer of indium-tin-oxide (ITO) which were first cleaned by exposing to air plasma for 10 minutes. After printing, the uncured resist on the substrate was dissolved and washed away in propylene glycol methyl ether acetate (PGMEA) by dipping the substrate into a bath of PGMEA for 10 minutes. The substrate was then cleaned by dipping into a clean bath of PGMEA for another 10 minutes. Without letting the substrate to dry, the printed structures were then photochemically cured to improve their mechanical properties (36, 37). This was achieved by transferring the structures into a 5% solution of Irgacure 651 in PGMEA and then exposing them to 365 nm UV light from a hand-held lamp for a period of 30 minutes. During exposure, the UV lamp with a power of 4 W was placed approximately a cm away from the printed structures. This photocuring step improves the mechanical properties of the printed structures and minimizes mechanical failure due to the capillary forces generated during drying. After this step, the substrates were washed by dipping in a clean bath of PGMEA for 5 minutes, then taken out of the liquid bath, and allowed to dry slowly overnight inside a confined container with minimal airflow to reduce the capillary forces.

2.4. Optical Simulations

The optical simulation technique is based on the model described in detail elsewhere (11). In summary, the light field in the focal volume was computed by simulating the propagation of a single broadband femtosecond pulse through the optical system. The propagation steps were mathematically represented using Fourier optics and computationally modelled using the MATLAB software package. The optical system comprises a 4f like arrangement of the collimating and objective lenses wherein the

surface of the DMD and the focal plane in the resist are conjugate planes of each other. The DMD was oriented with respect to the incident beam to achieve a blazed grating condition corresponding to the centre wavelength of the laser and the DMD micromirror pitch. The instantaneous intensity in the focal volume of the resist was simulated by first separately evaluating the electric field for each wavelength using monochromatic coherent optical models and then summing up the contribution of each wavelength. At each spatial location, the peak intensity was evaluated as the maximum value of this instantaneous intensity. The pulse width was evaluated by summing up all the time steps at which the instantaneous intensity exceeded half of the peak intensity. The optical dosage was evaluated by integrating the square of the instantaneous intensity with respect to time over the full duration of the simulation (i.e., 4 ps).

2.5. Simulation of Photopolymerization

Physics-based simulation of photopolymerization was performed via finite element modelling (FEM) of a set of reaction-diffusion partial differential equations. These equations model the kinetics of the radical quenching, polymer chain growth, and polymer chain termination reactions and the diffusion of the terminating species (oxygen) and free radicals generated from the photoinitiator molecules. The model was developed using the commercially available COMSOL multi-physics simulation package and it is based on our past work (38). The FEM model from literature was modified by updating the light dosage input and by calibrating the model parameters using empirical data from our custom-built P-TPL system. The light dosage input was updated to use the optical dosage per pulse as the input and the product of quantum yield and two-photon cross-section of the photoinitiator was calibrated from empirical data of P-TPL. The threshold degree of polymer conversion was also empirically

evaluated from Raman micro-spectroscopy of polymerized photoresist droplets that were polymerized using single-photon UV light illumination. Details of the reaction-diffusion equations and the calibration of the model using empirical data are available in the supplemental materials. The FEM simulations were performed for the same average power/pixel and printer configurations as that in the experimental set up.

2.6. General Characterization

Scanning electron micrographs were obtained on a Hitachi SU8010 scanning electron microscope (SEM) at 1 – 15 keV accelerating voltage. The printed samples were coated with a thin layer of gold (< 5 nm thick) before SEM imaging. Refractive index (RI) measurements were recorded on uncured photoresist material using a Mettler Toledo Excellence R4 refractometer. RI was measured at the D line of sodium (589 nm) at 20 °C. Raman micro-spectroscopy data were measured on a Renishaw inVia Qontor Raman micro-spectroscope. The degree of polymer conversion was evaluated from Raman micro-spectroscopy datasets using literature techniques (39), as discussed in detail in the supplemental materials.

3. Results and Discussion

3.1. Optical Proximity Effect from Light Projection

To quantify the optical source of the proximity effects, we have modelled the effect of feature density on the light dosage distribution in the focal volume. Our model captures the physics of electromagnetic wave propagation through the P-TPL optical system for the specific case of propagation of a single pulse of femtosecond light. The model was developed using Fourier optics techniques and it is based on the model presented in our previous work on P-TPL (11). Here, we have extended our previous work by evaluating

the pulse width (τ) , the peak intensity (I_p) , and the optical dosage per pulse (D_p) in the focal volume when the projections are varied. The optical dosage per pulse refers to the time integral of the square of the instantaneous intensity over the duration of the pulse. Therefore, it quantifies the net optical input to the photopolymerization process from each pulse.

As illustrated in Figure 2(c), we observe that upon projection of a patterned image, the optical dosage varies nonlinearly with the axial distance from the focal plane. For projection of a sparse image, the dosage decreases rapidly with increasing axial distance and it drops to less than 1% of the peak dosage within a distance of 1 µm from the focal plane. This stronger-than-linear axial gradient of dosage arises in P-TPL because both the temporal shape and the length of the femtosecond pulse varies along the axial direction. The pulse temporally resembles a Gaussian shape at the focal plane and it is also the shortest at that plane. However, the pulse broadens and its shape deviates away from the Gaussian shape as the axial distance from the focal plane increases. The pulse shape at the focal plane and away from it is illustrated in the supplementary material Figure S1. One would underestimate the axial gradient of the dosage if the variation in the shape of the pulse is not accounted for, as was performed previously while reviewing P-TPL (12).

The variation in the temporal pulse shape with axial distance can be explained through the temporal focusing mechanism of P-TPL, particularly when this focusing is applied to a structured light beam. It is well-known that during temporal focusing, the various wavelengths of light, that exist within the femtosecond pulse, arrive at the focal plane after traversing different optical paths (40-42). The optical path lengths for all wavelengths are equal only at the focal plane but the path lengths differ at planes away from the focal plane (40-42). For a fully illuminated image on the DMD, the different

wavelengths arrive at a given spatial position within the focal volume continually, one after the other. Temporal focusing of such a fully illuminated beam stretches the pulse at axial locations away from the focus but causes only minimal deviations from the Gaussian shape. In contrast, we observe here that upon projection of a structured image on the DMD, the different wavelengths from the different sections of the DMD arrive at a spatial location with temporal gaps, thereby, causing a change in the temporal shape of the pulse while simultaneously stretching it. These temporal gaps split an otherwise strong pulse into multiple weak pulses and this generates strongly nonlinear axial dosage gradients in P-TPL.

The dependence of the optical dosage distribution on the structure of the projected image suggests that this optical behaviour could be a source of the proximity effects observed during printing. We have verified that this optical behaviour is indeed a source of proximity effects by further investigating the effect of the density of features in the projected image on the dosage distribution in the axial and lateral directions. We have specifically studied this effect during projection of sets of periodic lines of a fixed width but with varying periods. The overall size of the image was held constant by changing the number of lines in the image. It can be deduced from Figure 3(a) that the background optical dosage along the axial direction depends strongly on the proximity of the line features, with a non-negligible finite background dosage existing at all planes for a fully illuminated image. Non-negligible finite background dosages also exist intermittently at some planes away from the focal plane for dense periodic line patterns. However, this background dosage becomes negligible for the sparse image. In contrast, the background dosage in the lateral direction is insensitive to the proximity of the lines because the dosage becomes identically zero at the non-illuminated points on the focal plane (Figure 3(b)). These observations can also be visually verified from the dosage

distribution shown in Figure 2(c). The presence of high axial background dosage during projection of dense images makes the printing more susceptible to over-polymerization defects because the background dosage may itself lead to some polymerization. Thus, optical contribution to the proximity effects in P-TPL makes it is challenging to achieve the printing of 3D structures with fine features and fine porosities.

We have overcome the challenge of printing fine features with fine porosities by leveraging: (i) the absence of background dosage on the focal plane and (ii) the dependence of the axial background dosage on the feature density. If a dense image is split into two or more non-overlapping sparse images and these images are then projected sequentially, the optical dosage on the focal plane resulting from one image will not add up with the optical dosage resulting from the other images. This is because the background dosage along the lateral direction, i.e., on the focal plane, is zero in the non-illuminated regions. Therefore, when considering exposures on the focal plane, the sequential projection scheme of P-TPL is similar to the serial point-by-point scanning scheme of conventional TPL. In both cases, the optical dosage is generated only in those regions which are directly exposed to light. However, the background dosage in planes away from the focal plane cannot be fully eliminated by splitting a dense image into sparse images. Nevertheless, the background dosage from each sparse projection will be lower than that from a single dense projection, as demonstrated in Figure 3. Thus, splitting the image into multiple sparse images broadens the operating window and makes it easier to achieve the printing of nanoporous 3D structures.

3.2. Chemical Proximity Effect from Polymerization Kinetics

Although splitting a dense image into sparser images reduces the background optical dosage, the proximity effects arising from the chemical kinetics of polymerization may

be sufficiently high to prevent printing of fine features with fine porosities. Therefore, to isolate the chemical sources of the proximity effects during P-TPL, we have computationally modelled the spatiotemporal evolution of polymerization through a set of coupled reaction-diffusion differential equations. These equations model the rate of the chemical reactions and the rate of diffusion of the chemical species.

It is generally considered that the chemical proximity effects during serial TPLbased printing of acrylate photopolymers arise from the reaction kinetics of the dissolved oxygen in the photoresist (21, 28). Oxygen plays a critical role in printing by quenching the photogenerated radicals and by terminating the growth of the polymer chains. The oxygen in the illuminated region is depleted due to its reactions with radicals. This causes oxygen from the immediate vicinity to diffuse into the illuminated region, thereby leading to a depletion of the oxygen in the immediate vicinity. At high scanning speeds, there is insufficient time for oxygen to diffuse in from a wider region and replenish the oxygen in and around the illuminated region. Thus, subsequent printing in the proximity of the previously printed region is poorly terminated, which leads to higher degree of polymer conversion (DOC) at the periphery of the features. This leads to features that are broader than those printed far away from other features. In contrast, at slow scanning speeds, oxygen is sufficiently replenished so that subsequent printing does not lead to broadening of features. It is worth mentioning here that the proximity effects may also arise from the diffusion of other chemical species that diffuse slower than O₂, such as the photoinitiator. However, the effect of such slowly-diffusing species has been observed to be negligible at the short ms time scales (26), i.e., on the time scales at which P-TPL operates. Therefore, here we have leveraged the reaction-diffusion kinetics of oxygen to control and minimize the chemical proximity effects in P-TPL.

We have minimized the chemical proximity effects in P-TPL by printing under process conditions that lead to low consumption of the dissolved oxygen so that the concentration of oxygen does not fall precipitously during the quenching and termination reactions. We have achieved these beneficial conditions by taking advantage of two distinct process modifications. First, we operate in a regime wherein the concentration of the primary radicals (species R*) generated from the photoinitiator molecules is significantly lower than the concentration of the dissolved oxygen (O₂) so that the consumption of O₂ is minimized. Second, we operate under conditions wherein the threshold degree of polymer conversion (i.e., DOC_{th}) that must be achieved to ensure successful prints is low.

The effect of these process modifications on the printing outcome was studied using FEM simulations. The results of these studies are summarized in Figure 4. One can observe that the DOC achieved at the centre of the features and in the vicinity is significantly higher for a hypothetical photoresist that has 20 times lower O2 concentration than a photoresist with realistic concentration of dissolved O2, even when the projected image remains unchanged (Figure 4(a) vs (b)). The numerical value for the realistic concentration of dissolved O2 was obtained from literature values of solubility of O2 in the photoresist (28). These studies demonstrate that it would be challenging to print porous 3D structures with a resist that has a low concentration of dissolved O2. In contrast, when O2 is held constant at a high value and the density of the features in the projected image is varied, comparable values of DOC are achieved at the centre of the features but higher DOC is achieved with a denser image on planes away from the focal plane (Figures 4(a) vs (c)). This distribution of DOC correlates with the optical dosage distribution shown in Figures 2 and 3. Thus, it can be deduced that at high O2 concentrations, the chemical source of the proximity effect is suppressed in P-

TPL and the printing outcome reflects the optical proximity effects. The optical proximity effects can be further suppressed by interspersing the line patterns, as evidenced by the reduction of the DOC at planes away from the focal plane in Figure 4(d) vs (c). This demonstrates the potential of interspersing P-TPL to achieve fine porosities.

It is noteworthy that whether the concentration of O₂ is 'high' or 'low' is determined by the relative concentration of the primary radicals R*. Here, we have achieved a high O₂ concentration by printing with a low photoinitiator (PI) molar concentration (= 1.65×10^{-3} mol dm⁻³), which was less than one-third the molar concentration of the dissolved O₂ in the photoresist. This stoichiometry of the photoresist components ensures that under no light exposure conditions can the local oxygen be depleted to zero. The concentration of PI used here is at least an order of magnitude lower than that generally used in conventional point-scanning TPL (27, 28). In addition, printing occurs with significantly lower number of fs pulses in P-TPL than in conventional serial TPL. For example, P-TPL can print features with 5-10 pulses whereas serial TPL scanning at a speed of 10 mm/s requires ~1000 pulses (11, 43). The lower number of pulses in P-TPL translates to lower initial concentrations of primary radicals and consequently this effect leads to lower oxygen consumption during printing. Under this condition, the diffusion of oxygen is suppressed due to lower concentration gradients. The net result is that the chemical proximity effect due to oxygen diffusion is suppressed.

We have further verified our claim of suppressed chemical proximity effects by explicitly tracking the spatiotemporal evolution of the concentration of O₂ in the illuminated region and in the non-illuminated (i.e., dark) region in the immediate vicinity of the illuminated region. The dark region refers to the region in which the

optical dosage per pulse falls below 1% of its peak value, i.e., the value at the centre of the line features. It can be observed from Figures 5(a) and (b) that for the case of high initial O₂ concentration (i.e., [O₂]_o), the concentration of O₂ in the non-illuminated regions remains within 94% of its initial value, and the concentration remains unchanged beyond a lateral and axial distance of 1 µm. Consequently, the spatiotemporal variations in the concentration of O₂ are negligibly small to generate any appreciable diffusion-based effects outside the illuminated region. In contrast, with a hypothetical photoresist that has a lower initial concentration of O₂, a significant drop in the concentration of O₂ is observed in the non-illuminated regions (Figures 5(c) and (d)). Interestingly, this drop is accompanied by rich dynamics of the local O₂ concentration evolution; for example, the O₂ concentration drops initially and then starts recovering at a later time. Such a behaviour indicates that subsequent printing in the non-illuminated region will be affected by prior printing through the chemical proximity effects. Thus, tuning the processing conditions to suppress the consumption of O₂ provides an effective means to suppress the chemical proximity effects.

We were able to achieve printing in P-TPL even at low concentrations of the primary radicals because the threshold DOC required to achieve printing was fairly low. It is well known that the threshold DOC is determined by two factors: (i) the DOC limit above which the polymer becomes insoluble in a solvent and (ii) the DOC limit above which the polymer becomes strong enough to survive the capillary forces that are generated during the solvent removal process (44). The second limit is higher than the first limit because the mechanical properties of the processed photoresist increases with increasing DOC (39, 45). Often, TPL printing processes are set up such that successful prints can be achieved only when the DOC exceeds the second limit (39, 46). However, we have explicitly devised our P-TPL printing and development processing steps so that

successful prints can be achieved even at DOC values lower than the second limit. We have achieved this by introducing an additional photochemical curing step during the development process. This curing process increases the DOC beyond that achieved from fs illumination alone, but it does not broaden the features. The post-print curing process is described in detail elsewhere (36, 37), and summarized in Section 2.3. This curing step ensures that one only needs to cross the DOC solubility limit to achieve printing. We have empirically measured the DOC solubility limit to be 7% for our photoresist (as described in detail in the supplemental material and illustrated in supplementary Figures S2 and S3). This DOC threshold is significantly lower than the values available in TPL literature which range from 16% to 60% (28, 46). It is noteworthy that the computationally evaluated as-printed DOC does not exceed 16% for the resist composition used here (Figure 4(a)) but it does exceed 16% for the hypothetical resist which has a lower concentration of O₂ (Figure 4(b)). Thus, without the photochemical curing step, printing via P-TPL would not have been possible under the current set of processing conditions. With this additional curing step, printing in P-TPL can be achieved at low radical concentrations which lead to low oxygen consumption and suppressed chemical proximity effects.

Although our FEM simulations were performed only for a limited set of conditions here, our results can be broadly generalized by developing an intuitive understanding of the underlying chemical dosage effects. Such an understanding can be developed by leveraging the unique time scale of P-TPL. In P-TPL, illumination occurs only for short ~100 fs durations followed by long durations of darkness on the scale of hundreds of µs. However, the dark period between subsequent fs pulses in conventional point-scanning TPL lasts only for ~10 ns (44). It is therefore customary to consider that photoactivated radicals are continually generated in serial TPL. This consideration

makes it challenging to decouple the dynamics of chemical dosage accumulation from chemical dosage decay. In contrast, the photoactivated radical generation and radical consumption steps in P-TPL can be distinguished in a time sequence and the dynamics of these processes can be better understood. For example, during P-TPL, the dynamics of chemical dosage can be tracked in terms of the rate of change of the concentration of the secondary radicals (P*), i.e., the radicals that are generated through cleavage of C=C bonds in the monomer molecules of the photoresist. Concentration of P* can increase only after new photoactivated primary radicals (i.e., R*) are generated through illumination; whereas, its concentration can decrease only through termination, primarily via reacting with dissolved oxygen. The concentration of P* remains unchanged during the cross-linking reactions that cause an increase in the DOC, as these reactions regenerate the radicals. Thus, chemical dosage accumulation from multiple pulses can be quantitatively tracked in terms of the increase in the concentration of P* whereas dosage decay can be tracked in terms of the decrease in concentration of P*. Additionally, the longer a finite value of P* exists at any material point, the higher the final DOC at that point would be. In combination, these three insights can be applied to rationally select processing conditions to minimize the chemical proximity effects.

For example, it can be observed from Figure 6 that the chemical dosage accumulates linearly with time and the peak dosage is proportional to the number of optical pulses. The increase in dosage due to each pulse is determined by the amount of light absorbed by the PI, its concentration, and the concentration of O₂. In contrast, dosage decays exponentially with time and the decay time constant is determined by the concentration of O₂. For the photoresist used in our experiments, this time constant is ~3 ms at the centre of the illuminated focal spot (Figure 6(a)), but the time constant

increases to >100 ms for the hypothetical resist with lower concentration of O₂ (Figure 6(b)). Details on the quantitative estimates of the time constant are available in the supplemental material. The final DOC is higher when either the time constant is higher or the maximum chemical dosage is higher. Reducing the concentration of primary radicals (i.e., R*) reduces both these parameters and leads to a reduction in the final DOC at any material point. With reduced DOC, the chemical proximity effects are minimized because the DOC in the regions away from the central point do not exceed the threshold DOC. Our approach of interspersing the line features takes advantage of this specific behaviour to minimize the chemical proximity effects.

3.3. Printing of Densely Packed Porous Structures

We have empirically demonstrated the ability to print dense 3D structures via P-TPL by printing various woodpile structures with pores and features smaller than 1 µm. The woodpiles were printed with a total of 40 layers each and the layers were spaced along the vertical z-axis by 900 nm. The layers were printed with a time-averaged power of 139 nW/px. The dosage per pulse corresponding to this average beam power is shown in Figure 3(a). Fine porosities were achieved by projecting a sequence of sparse images in each layer to minimize the optical proximity effects and by printing under those process conditions that minimize the chemical proximity effects. Specifically, we printed the woodpiles by projecting sequences of sparse periodic line pattern images comprising 5-pixel wide lines at a period of 30 pixels. As each pixel in the digital image maps to 113 nm in the physical projection, this period corresponds to a physical period of 3.4 µm. Periods finer than this value were achieved by interspersing the lines in one sparse image with the lines in another sparse image such that the resulting printed pattern has a lower period. We printed each layer by projecting two and three sets of

interspersed periodic line patterns to achieve 3D structures with nominal periods of 1.7 μm and 1.1 μm . Porous structures printed with three sets of interspersed lines are shown in Figure 7 and additional structures are shown in the supplementary material Figure S4.

As shown in Figure 7(b), projection of a pattern with 5-pixel wide lines and 10pixel period generated a fully-solid over-polymerized 3D structure that had no distinct line features. In contrast, projecting an image with a period of 30 pixels generated a porous 3D structure with distinct line features but pores bigger than 1 µm. This empirically verifies the presence of proximity effects in P-TPL. Interestingly, a nanoporous 3D structure with distinct line features could be obtained by projecting three images with 30-pixel periods and by interspersing the lines on the same plane. The nominal period of the composite interspersed image is 10 pixels and it is identical to that of the image projected to create the fully dense structure shown in Figure 7(b). The nominal period is the period in each sparse image divided by the number of interspersed sparse images (i.e., 30 pixels/3 images = 10 pixels). It can be verified that 3D structures with porosities smaller than 1 µm can be generated in both axial and lateral directions by interspersing P-TPL. Only the topmost layer was kept sparse in these prints to aid in SEM-based visualization of the porosities but all underlying layers were interspersed (as shown in Figures 7(e) and (f)). We achieved lateral porosities of less than 700 nm and features finer than 300 nm. These structures are significantly more closely packed, yet with distinctly separated features, than what had been printed in the past with P-TPL or what has been printed with projection techniques (11, 30). Although our experiments were limited to 3D lattice structures, we anticipate that the results of our studies can be applied to print other densely packed structures by interspersing the features across multiple projections and by minimizing the consumption of dissolved oxygen in the photoresist.

We have performed additional experiments to verify our FEA prediction that a photoresist with a lower concentration of dissolved oxygen will lead to higher chemical proximity effects. We created photoresists with lower concentrations of dissolved O₂ by degassing droplets of the photoresist for 30 and 60 minutes under a vacuum of 0.01 mbar. The degassing was performed immediately before printing with the resists. The degassing process reduces the concentration of the dissolved O₂ without affecting the concentration of the photoinitiator. Therefore, this set of experiments provides an unambiguous means to study the chemical proximity effects under varying O2 concentrations. As measuring the concentration of dissolved O2 in non-aqueous solutions is notoriously difficult (47), here we have not measured the O₂ concentration quantitatively. Instead, we rely on qualitative trends in the proximity effects arising from the decrease in the concentration of the dissolved O2 with increasing duration of degassing. The 3D structures generated with the degassed resists are shown in Figure 8. The results demonstrate that the proximity effects increase with a decrease in the concentration of the dissolved O₂. Under low O₂ concentrations, the proximity effects are severe enough to cause adjacent features to merge together. Thus, these experiments validate our FEA model predictions that the chemical proximity effects are more severe in a photoresist that has a lower concentration of dissolved O₂. It is noteworthy here that our approach of minimizing the chemical proximity effects by minimizing the consumption of dissolved O₂ is limited to acrylate-based photoresists wherein the polymerization reactions are terminated by the dissolved O₂. Nevertheless, we anticipate that our approach can be applied to a vast set of acrylate photoresists by tuning the monomer components to process a variety of polymers and polymer derived metals and ceramics (35, 48-50).

Although interspersing leads to a moderate reduction in the rate of printing by a factor of 2–3 times, the rate of interspersing P-TPL is still significantly higher than that of conventional point-scanning TPL. For example, each interspersed layer of size 800×515 pixels was printed here in 9.6 ms (=3.2 ms×3, with no time gap between the projection of the different images). This translates to a processing rate of 0.55 mm²/s per layer. The time to scan the same area sequentially at a high speed of 10-50 mm/s(21), and a period of 1 μ m along one direction is 526 ms – 105 ms, which corresponds to a sequential processing rate of 0.01-0.05 mm²/s per layer. Thus, interspersing P-TPL is more than 10-50 times faster than conventional point-scanning TPL. As such, the interspersing technique is effective in rapidly producing nanoporous 3D structures by leveraging the conditions that minimize the proximity effects in P-TPL.

Although an interspersing technique similar to ours has been demonstrated in the past to control the proximity effects in multi-point scanning-based TPL (20), our work demonstrates that the relative contributions of optical and chemical sources of proximity effects are significantly different in the projection-based versus scanning-based TPL. Here, we have demonstrated that the chemical proximity effects during P-TPL are suppressed due to the minimal consumption of dissolved O₂ in the photoresist under the low-pulse regime of P-TPL. Instead, the overall proximity effects in P-TPL are caused predominantly by the optical proximity effects arising from the light projection scheme. In contrast, past work by Arnoux et al. has demonstrated that diffusive chemical effects contribute significantly to the overall proximity effects in scanning-based TPL (20). In addition, their approach of minimizing the optical sources of the proximity effects by increasing the spacing between the adjacent multiple light spots does not have a direct analogy in P-TPL. This is because the spacing of adjacent pixels in P-TPL is fixed (at

113 nm here) and it is therefore not possible to avoid overlapping the light from adjacent pixels. Our work presented here demonstrates how the optical proximity effects can be minimized even in the presence of this additional constraint. Thus, our work clarifies those aspects of controlling the proximity effects in TPL that have not been discussed before.

It is important to note here that our demonstration of the interspersing technique was performed for those geometries in which the proximity effects arising from enhanced light absorption by previously polymerized material is minimized. However, our interspersing technique can be applied even for those cases in which the proximity effects due to enhanced light absorption by previously polymerized material are present. Here, we have specifically limited our interspersed printing operations to those geometries in which light from a focal spot did not illuminate any other already polymerized feature on the same layer. This was achieved by selecting the pattern period (1130 nm) to be higher than half of the sum of the width of the focal spot, i.e., the width above which the optical dosage per pulse drops below 0.1% of the peak dosage (1130 nm) and the width of the polymerized feature (300 nm). For features spaced closer than this limit (i.e., closer than 715 nm), the enhanced light absorption from the already polymerized material must also be considered to accurately predict the proximity effects. Nevertheless, our experiments show that the interspersed technique is capable of fabricating dense nanoporous 3D structures even without accounting for the proximity effects arising from enhanced light absorption by previously polymerized material.

4. Conclusions

Here, we have demonstrated that although it is challenging to print densely packed 3D

structures with P-TPL due to the proximity effects, these effects can be overcome through process modifications to achieve the desired printing. We demonstrate through physics-based computational models that the proximity effects can be distinctly separated into optical and chemical sources. The optical proximity effect can be overcome by minimizing the density of features in the projected image whereas the chemical proximity effect can be minimized by operating under process conditions that minimize the consumption of oxygen in the photoresist. We have also presented and validated a generalizable framework to quantitatively understand the chemical proximity effects in TPL via the dynamics of accumulation and decay of chemical dosage. Our framework predicts that the chemical proximity effects can be minimized by processing with a lower concentration of photoinitiator, fewer number of optical pulses, and a photoresist that has a low threshold degree of polymer conversion. We have leveraged these insights to devise a projection technique to print dense 3D structures by projecting an interspersing sequence of sparse images on the same plane. Our interspersing P-TPL technique enables printing of 3D woodpile structures with features thinner than 300 nm, porosities smaller than 700 nm, and at rates up to 50 times faster than conventional point-scanning TPL. Therefore, this work can enable the scalable manufacturing of deterministic nanoporous 3D structures for a wide variety of applications.

Acknowledgements

Funding from the U.S. National Science Foundation (NSF) CAREER award 2045147 is gratefully acknowledged. Imaging was performed at the Georgia Tech Institute for Electronics and Nanotechnology, a member of the National Nanotechnology Coordinated Infrastructure (NNCI), which is supported by NSF (ECCS-2025462).

Declaration of interest statement

The authors are co-inventors on pending and/or issued patents related to this work and the rights are assigned to either Georgia Tech Research Corporation or Lawrence Livermore National Security, LLC.

References

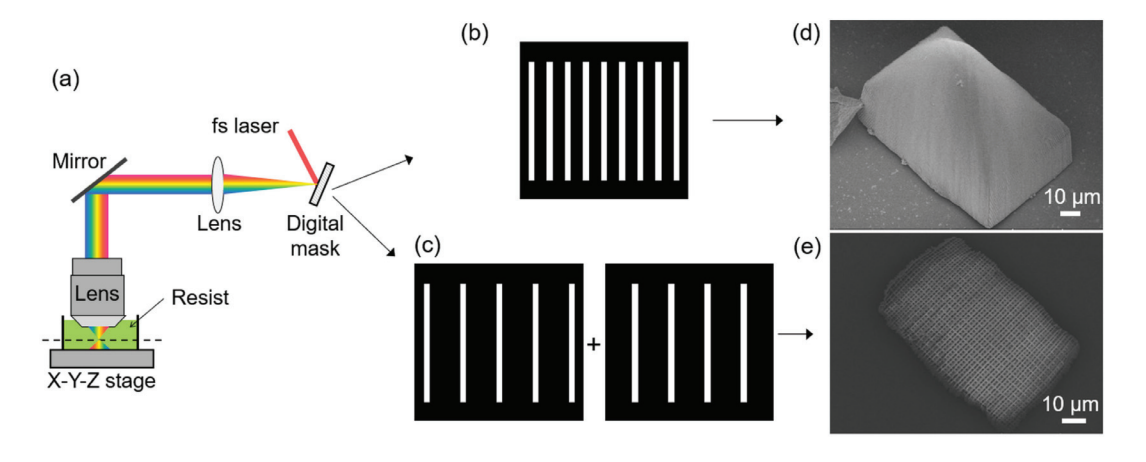
- 1. Meza LR, Das S, Greer JR. Strong, lightweight, and recoverable three-dimensional ceramic nanolattices. Science. 2014;345(6202):1322-6.
- 2. Bauer J, Meza LR, Schaedler TA, Schwaiger R, Zheng X, Valdevit L. Nanolattices: an emerging class of mechanical metamaterials. Advanced Materials. 2017;29(40):1701850.
- 3. Bauer J, Schroer A, Schwaiger R, Kraft O. Approaching theoretical strength in glassy carbon nanolattices. Nature materials. 2016;15(4):438-43.
- 4. Bauer J, Crook C, Izard AG, Eckel ZC, Ruvalcaba N, Schaedler TA, et al. Additive manufacturing of ductile, ultrastrong polymer-derived nanoceramics. Matter. 2019;1(6):1547-56.
- 5. Selimis A, Mironov V, Farsari M. Direct laser writing: Principles and materials for scaffold 3D printing. Microelectronic Engineering. 2015;132:83-9.
- 6. Torgersen J, Qin XH, Li Z, Ovsianikov A, Liska R, Stampfl J. Hydrogels for two-photon polymerization: a toolbox for mimicking the extracellular matrix. Advanced Functional Materials. 2013;23(36):4542-54.
- 7. Dietrich PI, Blaicher M, Reuter I, Billah M, Hoose T, Hofmann A, et al. In situ 3D nanoprinting of free-form coupling elements for hybrid photonic integration. Nature Photonics. 2018;12(4):241-7.
- 8. Moughames J, Porte X, Thiel M, Ulliac G, Larger L, Jacquot M, et al. Three-dimensional waveguide interconnects for scalable integration of photonic neural networks. Optica. 2020;7(6):640-6.
- 9. Gonzalez-Hernandez D, Varapnickas S, Bertoncini A, Liberale C, Malinauskas M. Micro-Optics 3D Printed via Multi-Photon Laser Lithography. Advanced Optical Materials. 2023;11(1):2201701.
- 10. Xia X, Afshar A, Yang H, Portela CM, Kochmann DM, Di Leo CV, et al. Electrochemically reconfigurable architected materials. Nature. 2019;573(7773):205-13.
- 11. Saha SK, Wang D, Nguyen VH, Chang Y, Oakdale JS, Chen S-C. Scalable submicrometer additive manufacturing. Science. 2019;366(6461):105-9.
- 12. Hahn V, Kiefer P, Frenzel T, Qu J, Blasco E, Barner-Kowollik C, et al. Rapid Assembly of Small Materials Building Blocks (Voxels) into Large Functional 3D Metamaterials. Advanced Functional Materials. 2020:1907795.
- 13. Cao C, Liu J, Xia X, Shen X, Qiu Y, Kuang C, et al. Click chemistry assisted organic-inorganic hybrid photoresist for ultra-fast two-photon lithography. Additive Manufacturing. 2022;51:102658.
- 14. Jonušauskas L, Juodkazis S, Malinauskas M. Optical 3D printing: bridging the gaps in the mesoscale. Journal of Optics. 2018;20(5):053001.

- 15. Carlotti M, Mattoli V. Functional Materials for Two-Photon Polymerization in Microfabrication. Small. 2019;15(40):1902687.
- 16. LaFratta CN, Baldacchini T. Two-photon polymerization metrology: Characterization methods of mechanisms and microstructures. Micromachines. 2017;8(4):101.
- 17. Sun H-B, Kawata S. Two-photon photopolymerization and 3D lithographic microfabrication. NMR• 3D Analysis• Photopolymerization: Springer; 2004. p. 169-273.
- 18. Wu S, Serbin J, Gu M. Two-photon polymerisation for three-dimensional microfabrication. Journal of Photochemistry and Photobiology A: Chemistry. 2006;181(1):1-11.
- 19. Skliutas E, Lebedevaite M, Kabouraki E, Baldacchini T, Ostrauskaite J, Vamvakaki M, et al. Polymerization mechanisms initiated by spatio-temporally confined light. Nanophotonics. 2021;10(4):1211-42.
- 20. Arnoux C, Pérez-Covarrubias LA, Khaldi A, Carlier Q, Baldeck PL, Heggarty K, et al. Understanding and overcoming proximity effects in multi-spot two-photon direct laser writing. Additive Manufacturing. 2022;49:102491.
- 21. Oakdale JS, Smith RF, Forien JB, Smith WL, Ali SJ, Bayu Aji LB, et al. Direct laser writing of low-density interdigitated foams for plasma drive shaping. Advanced Functional Materials. 2017;27(43):1702425.
- 22. Waller EH, Von Freymann G. Spatio-temporal proximity characteristics in 3D μ-printing via multi-photon absorption. Polymers. 2016;8(8):297.
- 23. Zheng L, Kurselis K, El-Tamer A, Hinze U, Reinhardt C, Overmeyer L, et al. Nanofabrication of high-resolution periodic structures with a gap size below 100 nm by two-photon polymerization. Nanoscale research letters. 2019;14(1):1-9.
- 24. Aderneuer T, Fernández O, Ferrini R. Two-photon grayscale lithography for free-form micro-optical arrays. Optics express. 2021;29(24):39511-20.
- 25. Kim H, Saha SK. Defect control during femtosecond projection two-photon lithography. Procedia Manufacturing. 2020;48:650-5.
- 26. Yang L, Münchinger A, Kadic M, Hahn V, Mayer F, Blasco E, et al. On the schwarzschild effect in 3D two-photon laser lithography. Advanced Optical Materials. 2019;7(22):1901040.
- 27. Sakellari I, Kabouraki E, Gray D, Purlys V, Fotakis C, Pikulin A, et al. Diffusion-assisted high-resolution direct femtosecond laser writing. ACS nano. 2012;6(3):2302-11.
- 28. Mueller JB, Fischer J, Mayer F, Kadic M, Wegener M. Polymerization Kinetics in Three-Dimensional Direct Laser Writing. Advanced Materials. 2014;26(38):6566-71.

- 29. Papagiakoumou E, Ronzitti E, Emiliani V. Scanless two-photon excitation with temporal focusing. Nature Methods. 2020;17(6):571-81.
- 30. Somers P, Liang Z, Johnson JE, Boudouris BW, Pan L, Xu X. Rapid, continuous projection multi-photon 3D printing enabled by spatiotemporal focusing of femtosecond pulses. Light: Science & Applications. 2021;10(1):199.
- 31. Saha SK, Chen S-C. Comment on "Rapid Assembly of Small Materials Building Blocks (Voxels) into Large Functional 3D Metamaterials". Advanced Functional Materials. 2020:2001060.
- 32. Hahn V, Wegener M. Response to "Comment on Rapid Assembly of Small Materials Building Blocks (Voxels) into Large Functional 3D Metamaterials". Advanced Functional Materials. 2020:2003402.
- 33. Rumi M, Ehrlich JE, Heikal AA, Perry JW, Barlow S, Hu Z, et al. Structure—property relationships for two-photon absorbing chromophores: bis-donor diphenylpolyene and bis (styryl) benzene derivatives. Journal of the American Chemical Society. 2000;122(39):9500-10.
- 34. Saha SK, Oakdale JS, Cuadra JA, Divin C, Ye J, Forien JB, et al. Radiopaque Resists for Two-Photon Lithography To Enable Submicron 3D Imaging of Polymer Parts via X-ray Computed Tomography. ACS Appl Mater Interfaces. 2018;10(1):1164-72.
- 35. Mettry M, Worthington MA, Au B, Forien J-B, Chandrasekaran S, Heth NA, et al. Refractive index matched polymeric and preceramic resins for height-scalable two-photon lithography. RSC Advances. 2021;11(37):22633-9.
- 36. Ladner IS, Cullinan MA, Saha SK. Tensile properties of polymer nanowires fabricated via two-photon lithography. RSC Advances. 2019;9(49):28808-13.
- 37. Kim H, Saha SK, editors. Minimizing Shrinkage in Microstructures Printed With Projection Two-Photon Lithography. American Society of Mechanical Engineers, International Manufacturing Science and Engineering Conference; 2022: American Society of Mechanical Engineers.
- 38. Pingali R, Saha SK. Reaction-Diffusion Modeling of Photopolymerization During Femtosecond Projection Two-Photon Lithography. Journal of Manufacturing Science and Engineering. 2022;144(2).
- 39. Oakdale JS, Ye J, Smith WL, Biener J. Post-print UV curing method for improving the mechanical properties of prototypes derived from two-photon lithography. Optics express. 2016;24(24):27077-86.
- 40. Oron D, Tal E, Silberberg Y. Scanningless depth-resolved microscopy. Optics express. 2005;13(5):1468-76.
- 41. Zhu G, Van Howe J, Durst M, Zipfel W, Xu C. Simultaneous spatial and temporal focusing of femtosecond pulses. Optics express. 2005;13(6):2153-9.

- 42. Choi H, Yew EYS, Hallacoglu B, Fantini S, Sheppard CJR, So PTC. Improvement of axial resolution and contrast in temporally focused widefield two-photon microscopy with structured light illumination. Biomedical optics express. 2013;4(7):995-1005.
- 43. Saha SK, Divin C, Cuadra JA, Panas RM. Effect of proximity of features on the damage threshold during submicron additive manufacturing via two-photon polymerization. Journal of Micro and Nano-Manufacturing. 2017;5(3).
- 44. Fourkas JT. Fundamentals of two-photon fabrication. Three-dimensional microfabrication using two-photon polymerization: Elsevier; 2020. p. 57-76.
- 45. Jiang LJ, Zhou YS, Xiong W, Gao Y, Huang X, Jiang L, et al. Two-photon polymerization: investigation of chemical and mechanical properties of resins using Raman microspectroscopy. Optics letters. 2014;39(10):3034-7.
- 46. Sun M, Cheng H, Golvari P, Kuebler SM, Yu X, Zhang M. Modeling of two-photon polymerization in the strong-pulse regime. Additive Manufacturing. 2022;60:103241.
- 47. Bakar NA, Abu-Siada A, Islam S. A review of dissolved gas analysis measurement and interpretation techniques. IEEE Electrical Insulation Magazine. 2014;30(3):39-49.
- 48. Vyatskikh A, Ng RC, Edwards B, Briggs RM, Greer JR. Additive manufacturing of high-refractive-index, nanoarchitected titanium dioxide for 3D dielectric photonic crystals. Nano letters. 2020;20(5):3513-20.
- 49. Vyatskikh A, Delalande S, Kudo A, Zhang X, Portela CM, Greer JR. Additive manufacturing of 3D nano-architected metals. Nature communications. 2018;9(1):1-8.
- 50. Bauer J, Crook C, Baldacchini T. A sinterless, low-temperature route to 3D print nanoscale optical-grade glass. Science. 2023;380(6648):960-6.

Figure 1



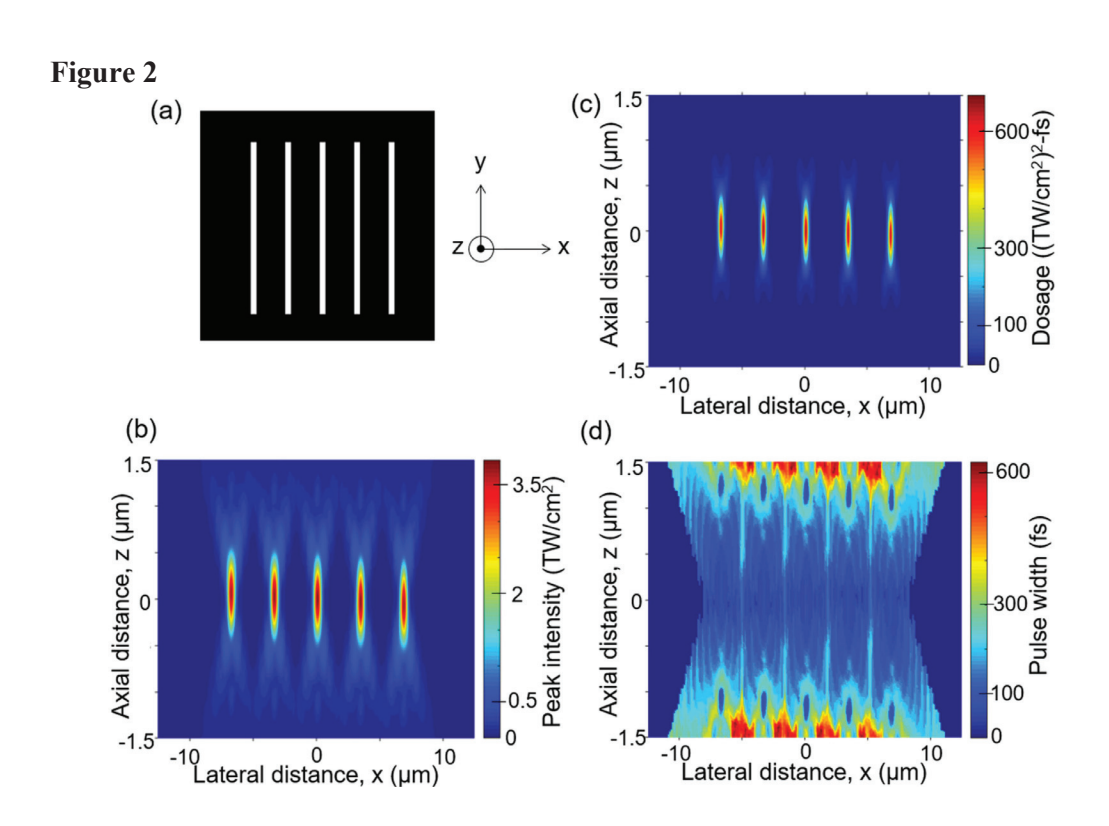


Figure 3

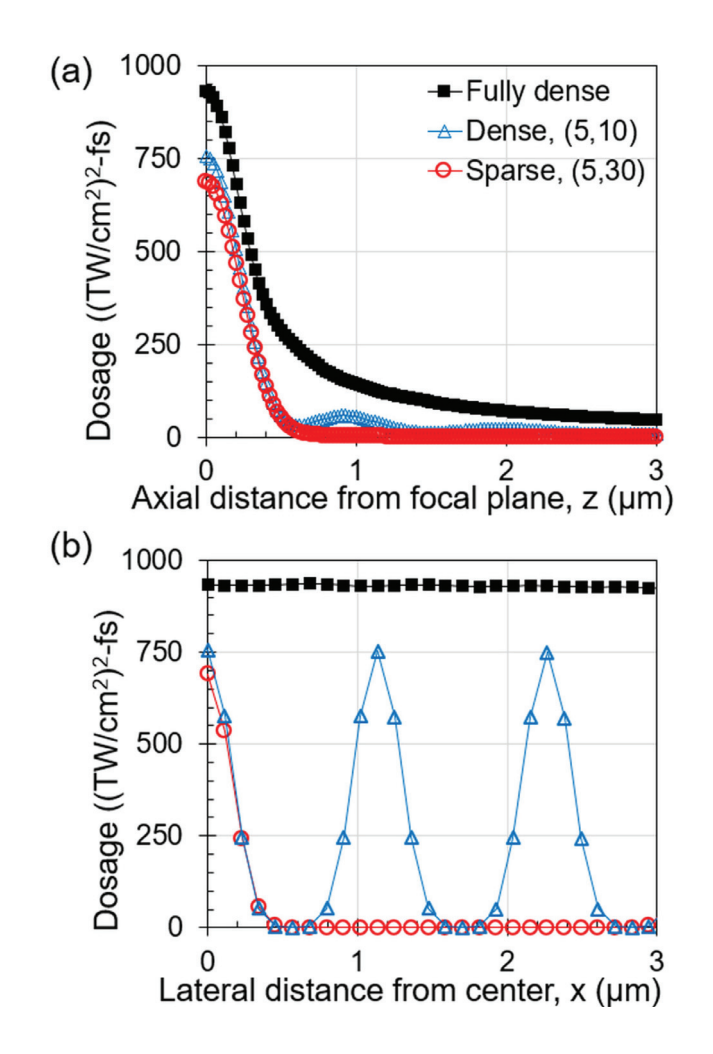


Figure 4

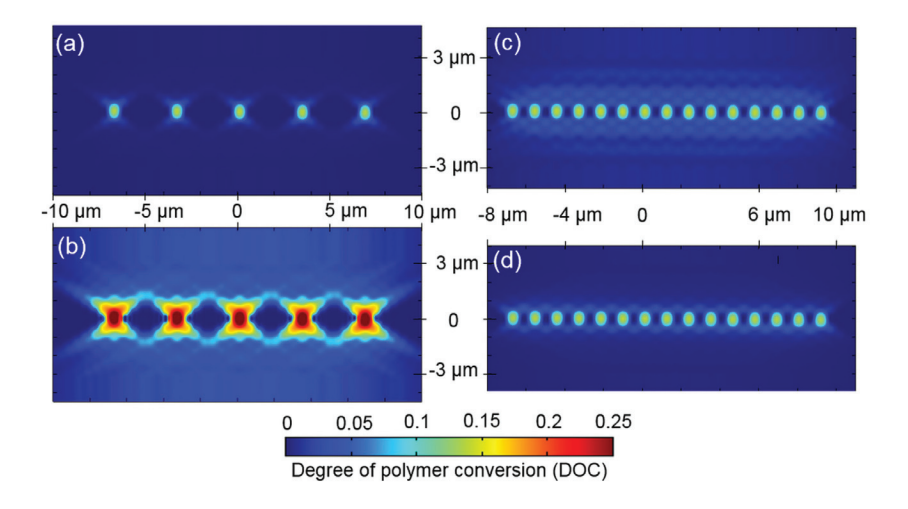


Figure 5

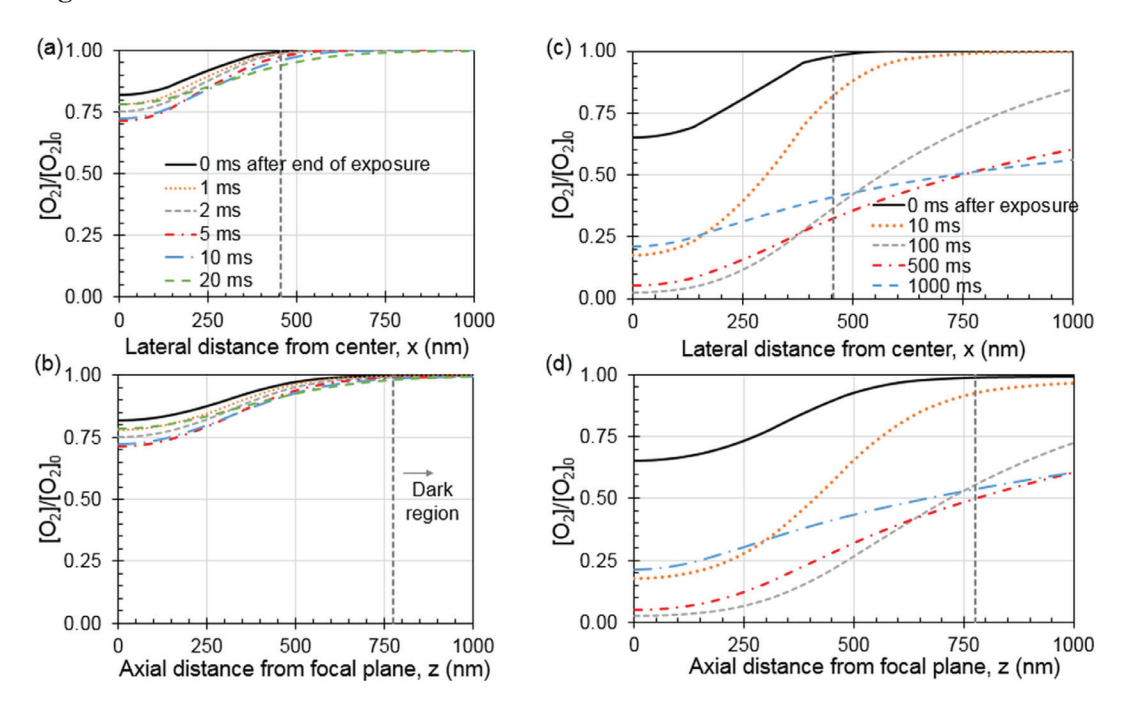


Figure 6

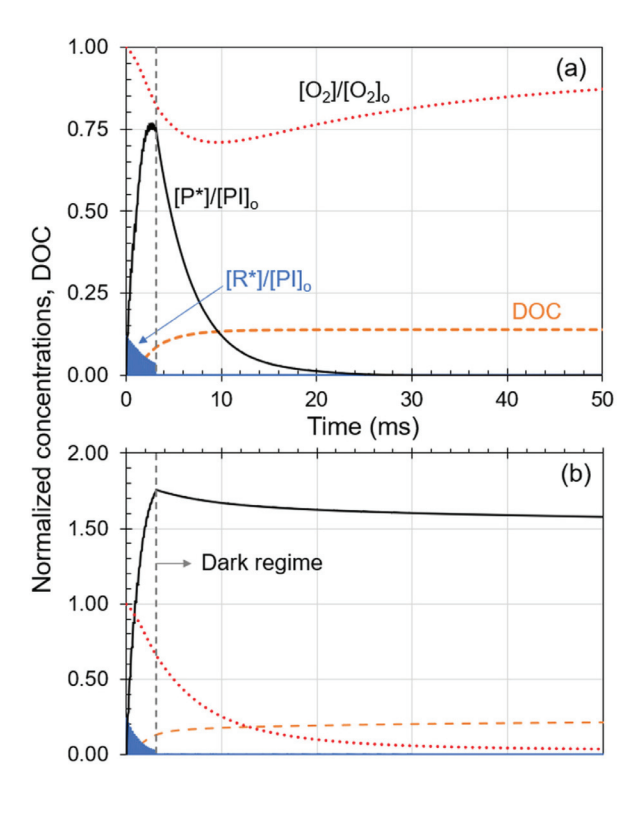


Figure 7

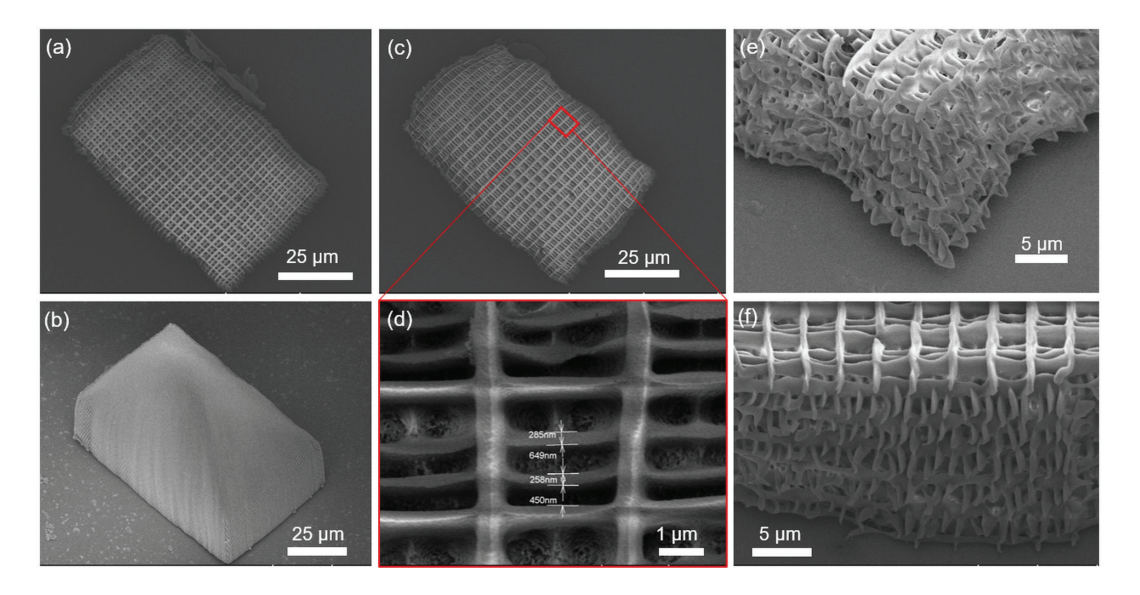


Figure 8

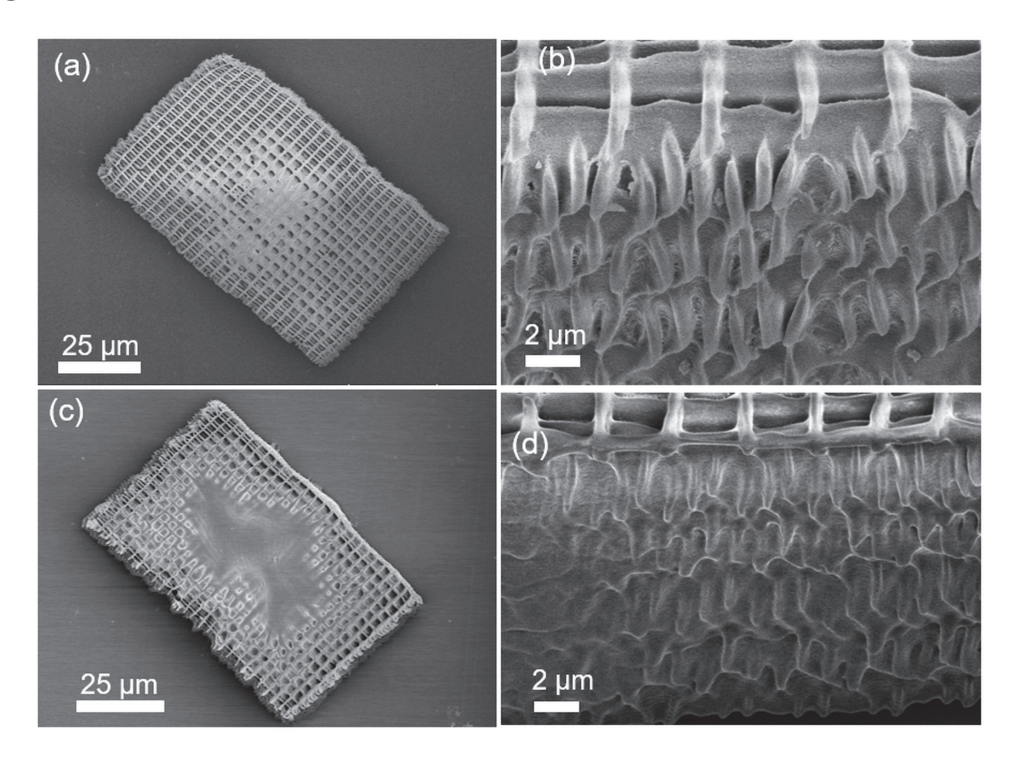


Figure Captions

Figure 1. (a) Schematic of projection two-photon lithography (P-TPL). (b) Densely packed digital image vs (c) two sparse images with interspersed line features that when superimposed generate a composite image identical to the dense image. (d) Scanning electron microscopy (SEM) image of a solid printed structure resulting from the projection of the dense image vs (e) nanoporous 3D structure resulting from the projection of the sequence of sparse interspersed images.

Figure 2: Computationally evaluated optical dosage profile for sparse vs dense projections. (a) Representative image of projected periodic line pattern. (b) Peak intensity distribution, (c) dosage per pulse, and (d) pulse width in the focal volume. Light propagates along the z-axis and a periodic line pattern comprising 5 lines of width 5 pixels and period 30 pixels was projected for (b)-(d). Each pixel maps to 113 nm at the focal plane.

Figure 3: (a) Dosage vs axial z-distance for three different projected images. (b) Dosage vs lateral x-distance for the same three projected images. (5,30) refers to sparse periodic line pattern image of 30-pixel period and 5-pixel linewidth whereas (5,10) refers to a dense image with 10-pixel period and 5-pixel linewidth. Fully dense refers to an image with all pixels illuminated. Each pixel maps to 113 nm at the focal plane.

Figure 4: Predicted degree of polymer conversion (DOC) under various projections and resist compositions generated from FEM. (a) For sparse periodic lines of 30-pixel period and 5-pixel width under realistic initial O₂ concentration of 6×10⁻³ mol dm⁻³. (b) For sparse periodic lines of 30-pixel period and 5-pixel width under low initial O₂ concentration of 3×10⁻⁴ mol dm⁻³. (c) For projection of dense lines of 10-pixel period and 5-pixel width. (d) For sequential projection of two interspersed sparse patterns of 20-pixel period and 5-pixel width. Initial O₂ concentration was 6×10⁻³ mol dm⁻³ for both (c) and (d). Each image was projected for 3.2 ms and the DOC was observed after it reached steady state (after 1000 ms for (b) and 200 ms for (a), (c), (d)). In (d), there was no time delay between the end of projection of the first image and the beginning of projection of the next image.

Figure 5: Spatiotemporal evolution of oxygen concentration in the vicinity of the center of the central line after exposure of a periodic line pattern of 30-pixel period and 5-pixel

width for a duration of 3.2 ms (i.e., 16 pulses). (a) and (b) for a photoresist with initial O_2 concentration (i.e., $[O_2]_o$) = 6×10^{-3} mol dm⁻³. (c) and (d) for a photoresist with $[O_2]_o$ = 3×10^{-4} mol dm⁻³.

Figure 6: Temporal evolution of the concentration of the chemical species at the centre of the central projected line upon illumination of a periodic line pattern of 30-pixel period and 5-pixel width for a duration of 3.2 ms (i.e., 16 pulses). (a) For a photoresist with realistic initial O₂ concentration (i.e., $[O_2]_o$) of 6×10^{-3} mol dm⁻³. (b) For a hypothetical photoresist with low initial O₂ concentration of 3×10^{-4} mol dm⁻³. $[PI]_o = 1.65 \times 10^{-3}$ mol dm⁻³ for both photoresists.

Figure 7: Woodpile 3D structures printed with sparse vs dense projections. (a) Porous structure with >1 μm lateral pores generated by projecting periodic line patterns of 30-pixel period and 5-pixel width for a duration of 3.2 ms per layer. (b) Solid structure generated by projecting a pattern with 10-pixel period and 5-pixel width for a duration of 3 ms per layer. (c) Nanoporous 3D structure generated by projecting three interspersed periodic line patterns in each layer wherein each pattern had a 30-pixel period and 5-pixel linewidth and was projected for 3.2 ms. (d)-(f) Close-up of top and side views of the nanoporous 3D structure (c).

Figure 8: (a) and (b) Top and side views of the mildly over-polymerized structure printed with the resist that was degassed for 30 min. (c) and (d) Views of severely over-polymerized structure printed with the resist that was degassed for 60 min. Both structures were generated by projecting three interspersed periodic line patterns in each layer wherein each pattern had a 30-pixel period and 5-pixel linewidth and was projected for 3.2 ms.

Supplementary Material for

Rapid printing of nanoporous 3D structures by overcoming the proximity effects in projection two-photon lithography

This PDF file includes:

Supplementary Text Figures S1 to S4 Table S1

S1. Pulse shape during temporal focusing

The shape of the temporally-focused femtosecond pulse at and near the focal plane is illustrated in Figure S1. It can be observed that the pulse resembles a Gaussian temporal shape at the focal plane for both structured (i.e., patterned) and unstructured (i.e., fully-illuminated) projections. However, the temporal shape of the pulse deviates away from the Gaussian shape at planes away from the focal plane. Furthermore, the intensity of the pulse intermittently drops to zero during projection of patterned light sheets. Therefore, a Gaussian pulse shape approximation is not accurate during projection of patterned light sheets.

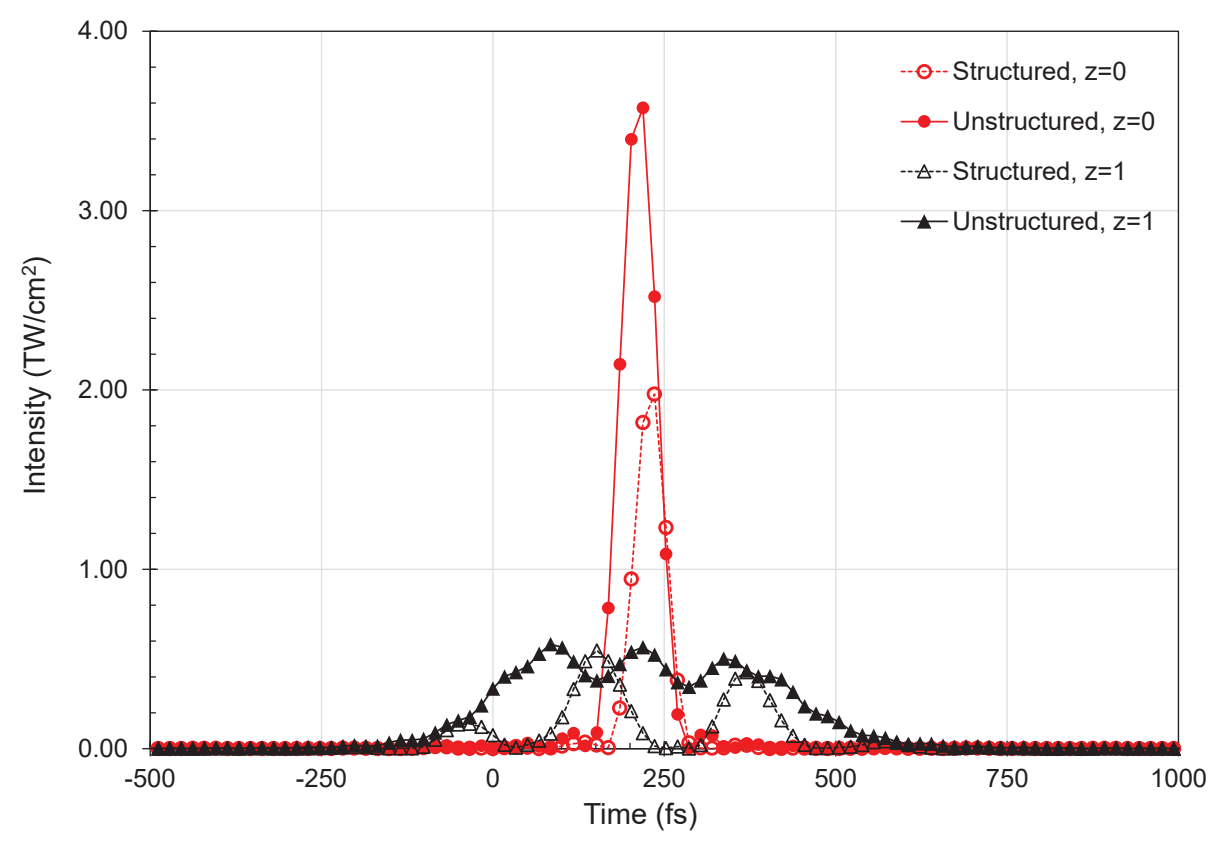


Figure S1: Pulse shape, represented as instantaneous intensity versus time, at the focal plane (z=0) and 1 μm away from the focal plane (z=1). 'Structured' projections were projections of periodic line pattern images comprising a total of 15 lines with a width of 5 pixels and a period of 10 pixels. 'Unstructured' projections were projections of 150-pixel wide fully-illuminated images.

S2. Finite element modeling of photopolymerization

S2.1. Model set-up

The finite element model implements a set of reaction-diffusion partial differential equations to represent the polymerization processes in P-TPL. The numerical model has been adapted from a previous work (38), and the key modifications to that model are described here. The parameters used for the numerical model are summarized in Table S1. The following set of partial differential equations represents the mathematical model that is solved using the finite element method:

$$\Delta[R^*] = \frac{D_p \sigma^{(2)} \Phi}{h^2 v^2} [PI] \tag{S1}$$

$$\frac{\mathrm{d}}{\mathrm{d}t}[\mathrm{R}^*] = -k_p[\mathrm{PETA}][\mathrm{R}^*] - k_q[\mathrm{O}_2][\mathrm{R}^*] + D_{\mathrm{R}^*} \left(\frac{\partial^2[\mathrm{R}^*]}{\partial x^2} + \frac{\partial^2[\mathrm{R}^*]}{\partial z^2} \right) \tag{S2}$$

$$\frac{\mathrm{d}}{\mathrm{d}t}[\mathrm{PETA}] = -k_p[\mathrm{PETA}][\mathrm{R}^*] - k_p[\mathrm{PETA}][\mathrm{P}^*] \tag{S3}$$

$$\frac{d}{dt}[P^*] = k_p[PETA][R^*] - k_t[O_2][P^*]$$
 (S4)

$$\frac{\mathrm{d}}{\mathrm{d}t}[O_2] = -k_q[O_2][R^*] - k_t[O_2][P^*] + D_{O_2} \left(\frac{\partial^2 [O_2]}{\partial x^2} + \frac{\partial^2 [O_2]}{\partial z^2} \right) \tag{S5}$$

$$\frac{\mathrm{d}}{\mathrm{d}t}[\mathrm{R}^{\mathrm{x}}] = k_q[\mathrm{O}_2][\mathrm{R}^*] \tag{S6}$$

$$\frac{\mathrm{d}}{\mathrm{d}t}[P^{\mathrm{x}}] = k_t[O_2][P^*] \tag{S7}$$

The square brackets represent the concentration of the chemical species within the bracket whereas the Δ symbol represents the change in the parameter. PI represents the photoinitiator, R* represents the primary radicals formed from the photoinitiator molecule, PETA represents the unreacted monomer, O₂ represents oxygen molecule, P* represents the secondary radicals formed through reactions with the monomer molecules, R* represents the dead primary radicals that cannot participate in further reactions, and P* represents the dead secondary radicals that cannot participate in further reactions.

Table S1: Model parameters and inputs to the model

Symbol	Parameter Name	Value	Source
$\sigma^{(2)}$	Two-photon cross section	133×10 ⁻⁵⁰ cm ⁴ s/photon-molecule	Estimate from Rumi et al. (Fig. 5, compound 8) (33)
h	Planck's constant	$6.626 \times 10^{-34} \mathrm{m}^2 \mathrm{kg} /\mathrm{s}$	Fundamental constant
K p	Polymerization rate constant	4.3×10 ⁴ dm ³ mol ⁻¹ s ⁻¹	Mueller et al. (28)
k_q	R* quenching rate constant	2.3×10 ⁶ dm ³ mol ⁻¹ s ⁻¹	
k _t	Termination rate constant	5.9 ×10 ⁴ dm ³ mol ⁻¹ s ⁻¹	Calibrated against empirical data
Ф	Quantum yield of photoinitiator	6.1×10 ⁻³	
DOC _{th}	Degree of conversion threshold	0.068	Determined through micro- Raman spectroscopy
D _{O2}	Diffusivity of oxygen	1.2×10 ⁻¹² m ² s ⁻¹	Estimated with Stokes- Einstein equation
D _{R*}	Diffusivity of R*	10 ⁻¹³ m ² s ⁻¹	
v	Optical frequency (central)	375 THz	Properties of laser in the printer
	Pulse repetition rate	5 kHz	
[O ₂] ₀	Initial O ₂ concentration (realistic level)	6 × 10 ⁻³ mol dm ⁻³	Mueller et al. (28)
	Initial O ₂ concentration (hypothetical low level)	3 × 10 ⁻⁴ mol dm ⁻³	5% of realistic level
[PI] ₀	Initial photoinitiator concentration	1.65 × 10 ⁻³ mol dm ⁻³	Resist composition, PI at 0.1% by weight
[PETA] ₀	Initial monomer concentration	4.0 mol dm ⁻³	Material datasheet for PETA

S2.2. Optical dosage input to the model

While the prior version of the model used the time-averaged intensity of the projected light field and the pulse duration at the focal plane as the optical dosage input to the finite element model (38), the current version of the model uses the optical dosage per pulse (D_p) as the input to the model. This modification accurately captures the effect of the spatiotemporally varying instantaneous intensity and avoids the error from space and time averaging. A scheme to decrease the amount of photoinitiator remaining after each pulse was also implemented. The product of the two-photon cross-section and the quantum yield of the photoinitiator molecule was empirically calibrated. The two-photon cross-section was estimated from literature for the illumination center wavelength of 804 nm (33). The quantum yield can then be estimated from the calibrated product of two-photon cross-section and quantum yield. These values are listed in Table S1.

S2.3. Empirical determination of the threshold degree of polymer conversion (DOC_{th})

We have empirically determined the DOC_{th} as the DOC value at which the photopolymerized resist transitions from being soluble to becoming insoluble in the solvent that is used during the P-TPL development process. For these experiments, single-digit mm-scale droplets of the photoresist were exposed to varying durations of UV light at a fixed intensity. Irgacure 651 was used as the photoinitiator in the resist. After exposure, the droplets were submerged in the solvent propylene glycol monomethyl ether acetate (PGMEA) for 10 minutes and then washed in a bath of isopropanol for 10 minutes. The droplets were then visually observed to identify whether any solidified material remained (outcome '1') or whether the entire droplet dissolved ('outcome 0'). The results of these studies are shown in Figure S2.

From Figure S2, it can be seen that a UV exposure of 10 minutes is necessary to cross the threshold DOC. The DOC of the 10-minute sample was measured through micro-Raman spectroscopy, which is a widely-used technique for determining the DOC in samples fabricated by two-photon polymerization (39, 45). Measurements were taken at several depths within the polymerized droplet and the DOC was averaged over the depth. This yielded a DOC_{th} value of 6.8% for the monomer blend used in this study. A representative spectrograph that was obtained from the micro-Raman measurements is shown in Figure S3. The DOC was calculated from the ratio between the areas of the C=C and C=O peaks in the unpolymerized and polymerized samples. As the number of C=O peaks does not change during polymerization, the intensity of the C=O peaks are used to scale the two spectrographs. Upon rescaling, the change in the intensity of C=C peaks represents the change in the number of C=C bonds, i.e., the degree of polymerization. This is mathematically represented as:

$$DOC = 1 - \left(\frac{A_{C=C}/A_{C=O}}{A'_{C=C}/A'_{C=O}}\right)$$
 (S8)

Here, the A_x parameters represent the area under the peak for the x bond, the parameters in the numerator of the second term on the right-hand side represent the parameters for the cured sample and the parameters in the denominator represent the parameters for the uncured sample.

S2.4. Empirical calibration of rate constant k_t

The model was calibrated against empirical data generated from printing of 7-pixel wide lines printed with 3 and 4 pulses of light exposure. The corresponding linewidths were measured to be 207 nm and 414 nm. The calibrated k_t value is listed in Table S1.

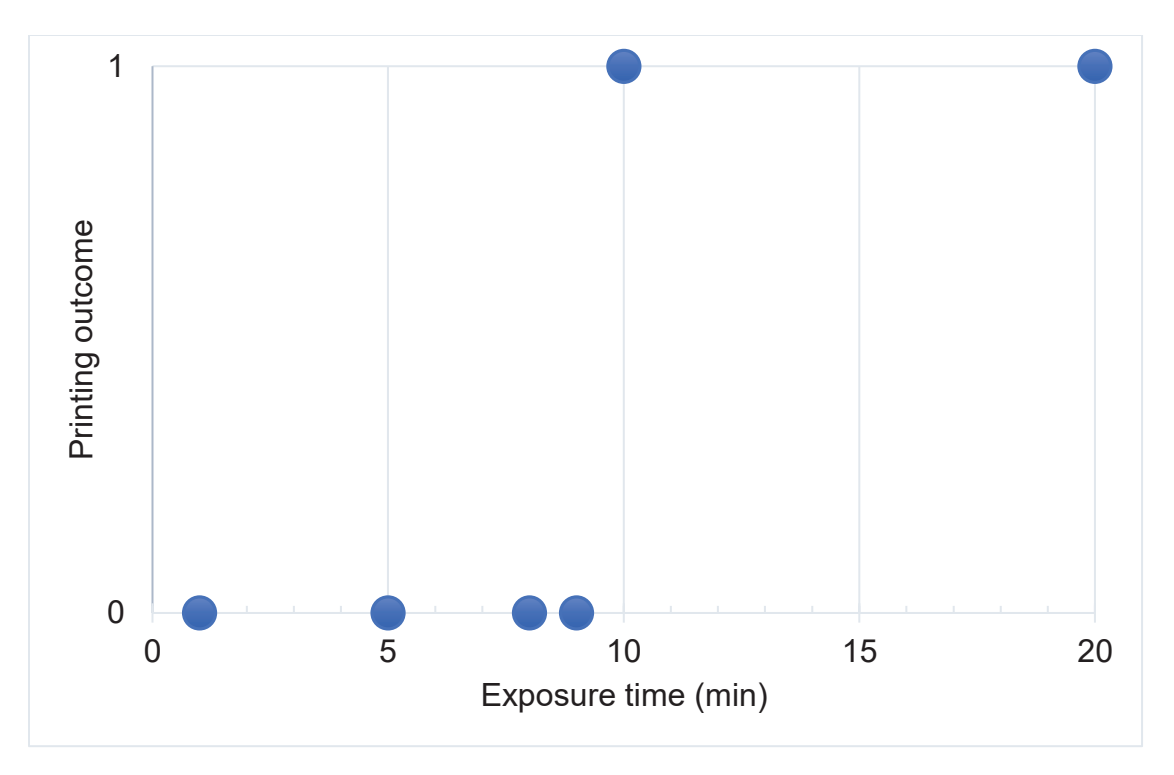


Figure S2: Presence or absence of printing under flood UV exposure for different durations of exposure.

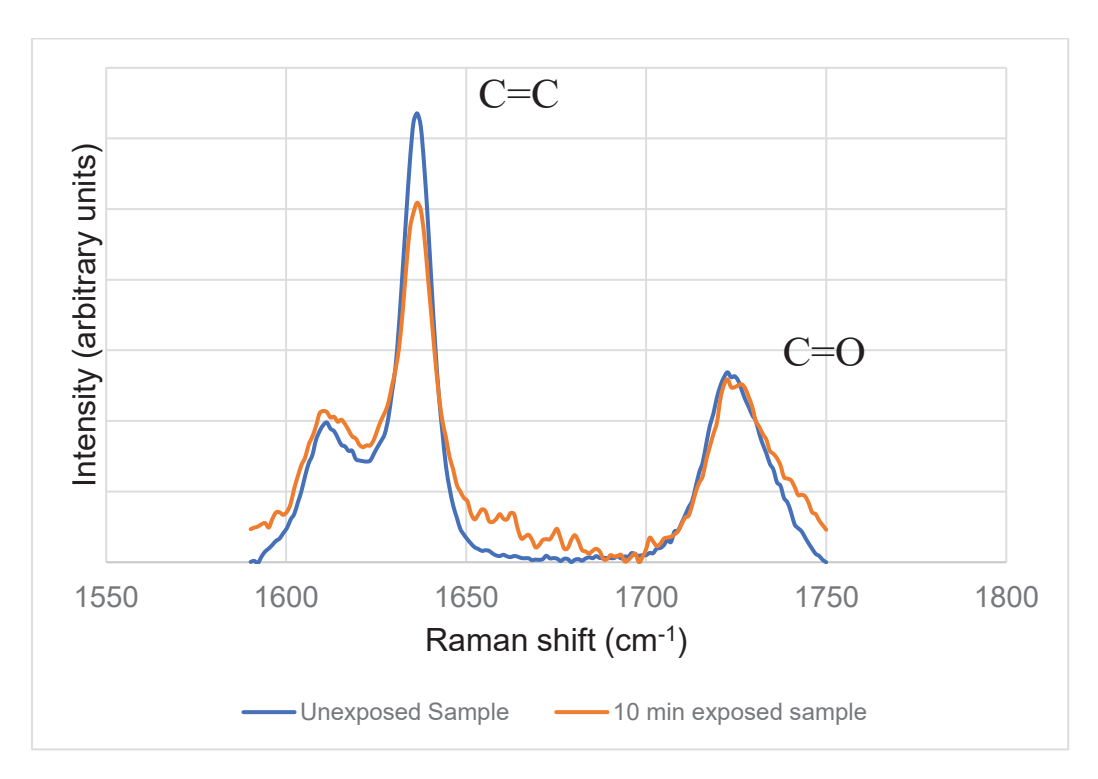


Figure S3: Micro-Raman spectrographs for droplet of monomer blend ('Unexposed sample') and polymerized droplet exposed to 10 minutes of flood UV exposure ('10 min exposed sample').

S2.5. Estimation of decay time constant during decay of [P*]

The decay in the concentration of the secondary radicals (i.e., P*) occurs via termination of these radicals with oxygen, as represented by the second term on the right-hand side of Equation S4. Therefore, upon simplifying this equation, the rate of decay of P* can be represented as:

$$\frac{\mathrm{d}}{\mathrm{d}t}[P^*] = -k_t[O_2][P^*] \tag{S9}$$

For the case when the concentration of oxygen does not precipitously fall, one may consider $[O_2]$ as a constant with respect to time. Under this approximation, Equation S9 reduces to an exponential decay equation with the decay time constant $\tau = 1/(k_t [O_2])$. The decay constant represents the time at which $[P^*]$ reduces to 1/e times its peak value (i.e., the value at time t=0). Upon substituting the values for oxygen concentration $[O_2] = 6 \times 10^{-3}$ mol dm⁻³ and $k_t = 5.9 \times 10^4$ dm³ mol⁻¹s⁻¹, the decay time constant $\tau = 3$ ms. This estimate is close to the value of τ (= 4 ms) as measured from Figure 6(a).

S3. Parametric studies of P-TPL during printing of woodpiles

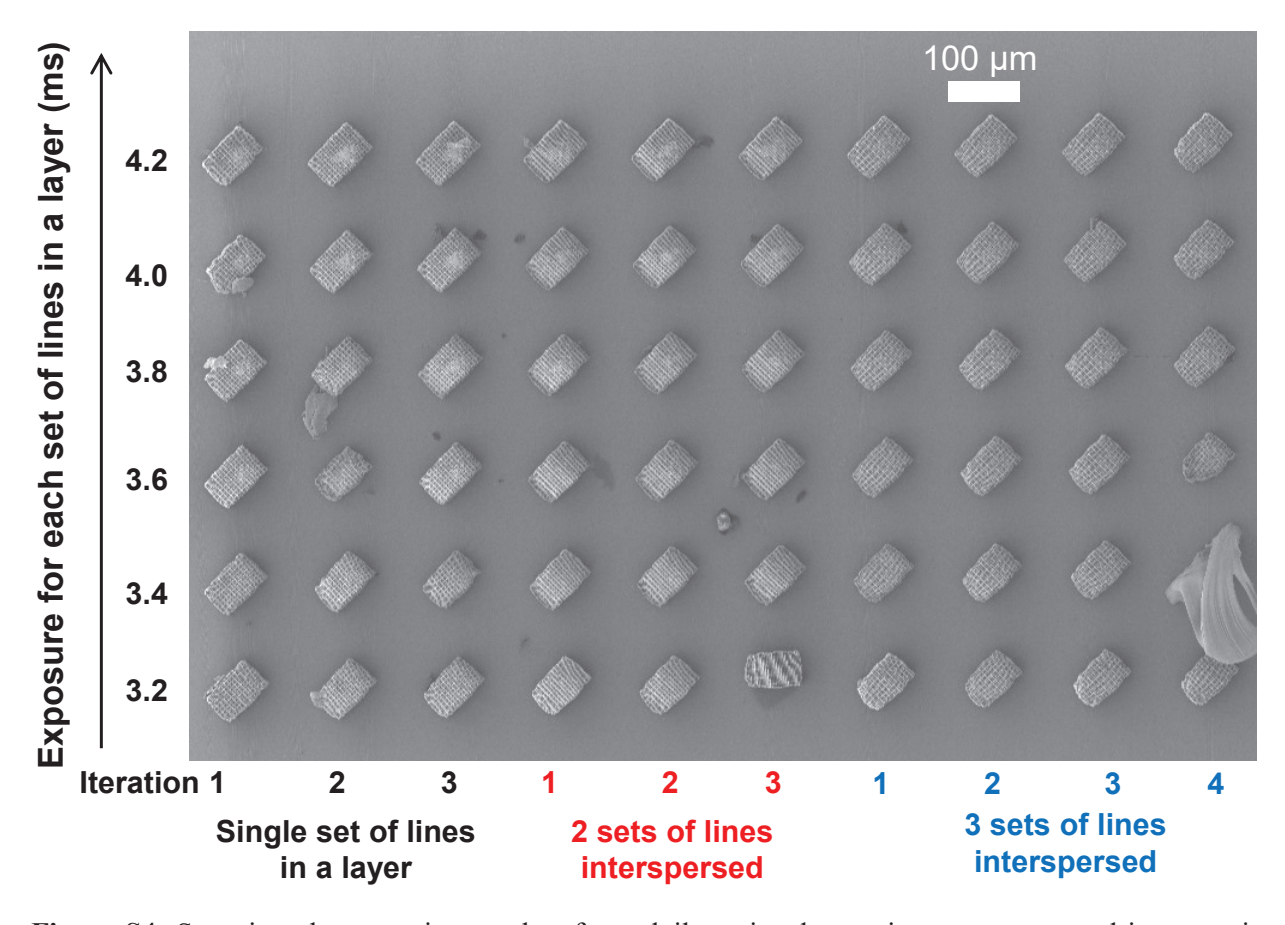


Figure S4: Scanning electron micrographs of woodpiles printed at various exposures and interspersing techniques. Three-to-four replicates were printed for each combination of parameters. In each layer, periodic line patterns had a period of 30 pixels and contained 5-pixel wide lines. The length of the projection was 800 pixels and the width was 515 pixels. Upon projection, each pixel was mapped to 113 nm at the focal plane. Each structure comprised a total of 40 layers and the layers were stacked vertically at a spacing of 900 nm. After exposing each layer, the z-stage was moved from one layer to the next layer within 12 ms.